Robust Automated Stopping Criterion for Semi-Convergent Image and Velocity Reconstruction in Electrical Capacitance Volume Tomography

SHAH M. CHOWDHURY [1,2] **(Member, IEEE), CODY PARK** [3] **, YASWANTH POTTIMURTHY** [3] **,**
QUSSAI M. MARASHDEH [4] **(Senior Member, IEEE), FERNANDO L. TEIXEIRA** [1,2] **(Fellow, IEEE),**
AND LIANG-SHIH FAN [3]

[1]ElectroScience Laboratory, The Ohio State University, Columbus, OH 43212, USA

[2]Department of Electrical and Computer Engineering, The Ohio State University, Columbus, OH 43212, USA

[3]Department of Chemical and Biomolecular Engineering, The Ohio State University, Columbus, OH 43214, USA

[4]Tech4Imaging LLC, Columbus, OH 43220, USA

CORRESPONDING AUTHOR: S. M. CHOWDHURY (e-mail: chowdhury.79@osu.edu)

This work was supported in part by the Department of Energy (DoE) under Grant DE-SC0018758.

ABSTRACT Electrical Capacitance Volume Tomography (ECVT) is a low-cost and high-speed sensing modality with great potential for industrial multiphase flow monitoring. In this work, we examine the use of the slope of the capacitance vector residual curve, as directly provided by the measurement data, to formulate a robust stopping criterion for the iterative image reconstruction in ECVT. The methodology is illustrated based on experimental data from a gas-solid fluidized bed. We show that the proposed stopping criterion can improve the performance of both the image reconstruction and the flow velocity profiling in ECVT applications. For concreteness, we focus on the popular Landweber iterative reconstruction algorithm although other reconstruction algorithms exhibiting semi-convergent behavior might benefit from the present analysis as well.

INDEX TERMS Capacitance tomography, fluidized bed, landweber iteration, multiphase flow, velocity profile.

I. INTRODUCTION

ELECTRICAL capacitance volume tomography (ECVT) has emerged in recent years as a promising multiphase flow monitoring tool for industrial applications. ECVT performs high-speed volumetric image reconstruction and velocity profiling of the flow media based on mutual capacitance measurements [1], [2]. Through imaging and velocimetry, it is possible to achieve a greater insight into flow characteristics such as chemical reaction, heat and mass transfer etc., enabling process optimization and increased production. ECVT has been applied in the investigation of fluidized beds [3]–[6], trickle beds [7], slurry bubble columns [8], phase separators [9] and various other industrial processes that are extensively used in petroleum,

pharmaceutical, metallurgical, energy and water treatment industries. It should be noted that ECVT finds its origin in electrical capacitance tomography (ECT), a two-dimensional imaging modality based on capacitance sensors [10]–[12]. As such, many algorithms developed for ECT can be directly translated to ECVT, e.g., the Landweber iterative algorithm for image reconstruction [13], [14].

An ECVT sensor is comprised of metal electrodes mounted around an insulating pipe containing the flow media. The electrodes are arranged in multiple layers which enables volumetric imaging. One of the major advantages of ECVT is its non-intrusive operation. This allows uninterrupted and safe operation of the plants, as opposed to intrusive techniques such as pressure sensors and wire-mesh

sensors [15], which may require periodic maintenance to prevent corrosion and clogging of the electrodes. Other advantages of ECVT include fast acquisition rate, conformal sensor shape, lightweight, low-cost, and the ability to operate under harsh industrial conditions such as high temperature and pressure. This characteristics make ECVT be often preferred over bulky and costly imaging modalities such as X-ray CT and magnetic resonance imaging (MRI). On the other hand, ECVT image resolution is lower compared to X-ray CT and MRI. ECVT resolution can be improved with adaptive ECVT sensors and electronic scanning [16] at the cost of greater hardware complexity and lower acquisition speeds.

Although capable of flow imaging, there has been no robust flow velocity profiling method based on ECVT apart from [2]. In that work, velocity reconstruction is obtained based on the gradient of the sensitivity map. Although this obviates the need for any image cross-correlation (as found in earlier ECT-based velocimetry approaches), the proposed velocity reconstruction method is highly dependent on the outcome of the image reconstruction step; in other words, any inaccuracy in the latter affects the former significantly. One such issue is the occurrence of unreasonably high velocity estimates caused by under-reconstructed images when a flow phase exists in very low volume fractions. A primary challenge related to this issue is *semi-convergence* of iterative image reconstruction algorithms, i.e., the fact that when applying such algorithms to an ill-posed reconstruction problem (such as ECT and ECVT), the improvement in image quality is not monotonic: the quality improves initially but after some iterations it starts to deteriorate [17]–[19]. Consequently, it is of key importance to determine a good stopping criterion for iterative algorithms.

In this work, we examine the use of the slope of the capacitance vector residual curve, as directly provided from the measurement data, to formulate a robust stopping criterion for the iterative image reconstruction algorithm in ECVT. For concreteness, we focus on the Landweber iterative algorithms because of its wide adoption in practice, although other semi-convergent iterative image reconstruction algorithms might benefit from the analysis presented here as well.We show that such a stopping criterion can improve the performance of both the image reconstruction and the velocity profiling in ECVT applications. The stopping criterion is implemented based on observations that are dependent on the sensor configuration, such as electrode shape and number, and flow materials. A change in either of these may require adjustments to the criterion, however, a change in flow regime, such as from slug to bubbly, should not affect it. The methodology is illustrated based on experimental data derived from [20], which consists of gas-solid fluidized bed experiments including both high and low solid volume fraction scenarios. Another dataset from the same experiment but with different sensor position is used for verification of the method.
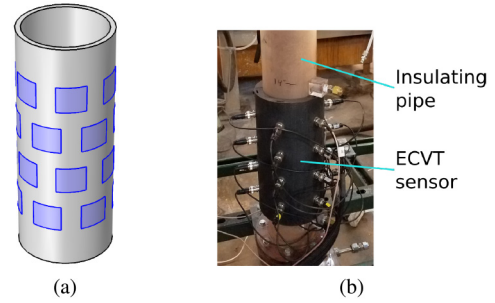
FIGURE 1. (a) A 24-electrode staggered ECVT sensor model arranged in a 6 × 4 configuration. Sensor diameter is 114 mm and length is 216 mm. (b) The actual ECVT sensor mounted on a pipe and wires connected.

The remainder of the paper is organized as follows. In Section II, the image and velocity reconstruction procedure for ECVT is briefly described, along with a formulation of the proposed robust stopping criterion. In Section III, the experimental setup is described first, followed by the issues created due to the lack of a stopping criterion with the image reconstruction method. Then, the stopping criterion based on the slope of the capacitance residual curve is illustrated, followed by how it improves the overall performance. After that, the developed automated stopping procedure is verified based on an additional dataset derived from the same experiment but with a different flow regime. In Section IV, the main findings are summarized.

II. METHODOLOGY
A. IMAGE RECONSTRUCTION

Fig. 1(a) shows a staggered 24-electrode ECVT sensor model mounted on an insulating pipe and Fig. 1(b) shows the corresponding physical sensor. The electrodes are arranged in four layers with six electrodes in each layer. Such a sensor is capable of sensing the dielectric materials within the cylindrical volume covered by the electrodes, called the region of interest (RoI). Cylindrical shaped sensors are the most common, however, cubic [21] and planar [22] shaped sensors are also investigated for specific purposes. The number of electrode pairs for an *n*-electrode sensor is given as $M = \binom{n}{2} = \frac{n(n-1)}{2}$, which is 276 for a 24-electrode sensor. This corresponds to the number of measurements, arranged in a $C_{M \times 1}$ measurement vector.

A $21 \times 21 \times 21$ discretization is used here for imaging the region of interest (RoI). This results in $N = 6300$ voxels inside the cylindrical RoI arranged in a $g_{N \times 1}$ permittivity vector. The forward transformation is defined as $C = T(g)$, for which a commonly used linearized model is given as

$$C = Sg \qquad (1)$$

where $S_{M \times N}$ is the sensitivity (Jacobian) matrix [23]–[25]. Each row of S corresponds to a mutual capacitance pair, whereas each column corresponds to a voxel. Here, sensitivity refers to the change in capacitance due to a perturbation in permittivity in the RoI. For image reconstruction, the capacitance vector C is normalized with respect to empty

and full vessel measurements, as described in [25]. Two types of normalizations are possible: regular and inverse, which highlight the high and the low permittivity phases, respectively. Normalization plays an important role in velocity reconstruction, such as regular normalization highlights the velocity profile with the high permittivity solid phase, whereas inverse normalization highlights the velocity profile with the low permittivity gas phase. Here, empty and full vessel is defined as the vessel being filled homogeneously with low and high permittivity media respectively.

A direct inverse does not exist for (1) because the problem is highly under-determined, i.e., $M \ll N$. A pseudo-inverse can be expressed as $\hat{\boldsymbol{g}} = \boldsymbol{S}^{\dagger}\boldsymbol{C}$. The system is also ill-posed, i.e., the inverse problem is highly sensitive to measurement noise, which requires regularization [26]. Methods used for ECVT image reconstruction include truncated singular value decomposition (SVD), Tikhonov regularization [27], Landweber iteration [13], [14], neural network based optimization [28]. Landweber iteration is adopted here for its simplicity and proven effectiveness [29]. This is a steepest gradient descent based method, expressed as

$$\hat{\boldsymbol{g}}_{k+1} = \hat{\boldsymbol{g}}_k - \alpha \boldsymbol{S}^T\left(\boldsymbol{S}\hat{\boldsymbol{g}}_k - \boldsymbol{C}\right) \tag{2}$$

where k is the iteration number and α is the step length chosen to be a constant subject to $0 < \alpha < 2/\sigma_1^2$, σ_1 being the largest singular value of $\boldsymbol{S}$. The term $2/\sigma_1^2$ is referenced as $\alpha_{\max}$ later. Both k and α are considered as regularization parameters, which can be tuned to influence the image reconstruction quality and speed. The initial guess $\hat{\boldsymbol{g}}_0$ can be obtained from the non-iterative linear back projection (LBP) method expressed as $\hat{\boldsymbol{g}}_0 = \boldsymbol{S}^T\boldsymbol{C}$.

B. STOPPING CRITERION FOR LANDWEBER ITERATION METHOD

Iterative methods for ill-posed problems are semi-convergent, which means the image quality improves up to a certain iteration, then starts to decrease. Some empirical knowledge of this optimum iteration number is required for specific flow types. Typical flow patterns include slug, annular, core, bubbly, etc. This strategy is not very robust because a change in the flow pattern would require resetting the iteration count. Another disadvantage of this fixed iteration count method is that low volume fraction[1] frames remain under-reconstructed, causing the velocity reconstruction method to under-perform. Low volume fraction frames typically require a larger number of iterations for proper reconstruction as compared to high volume fraction frames, assuming that a fixed step length α is used in both cases. As a result, the former may remain under-reconstructed if the iteration count is set for the latter, which is the usual case. This results in unreasonably high velocity magnitudes with the reconstructed velocity profile.

---

[1]. The volume fraction (or simply fraction) of a phase is defined as the ratio of the volume of that phase to the whole volume of the vessel.

```
1:  procedure LANDWEBER(C,S)
2:      Import capacitance norm ||C|| to fraction of α_max map,
        referred as Map 1
3:      Import capacitance norm ||C|| to magnitude of the slope of
        the capacitance residual (CR) map, referred as Map 2
4:      Determine 2-norm of capacitance vector C, n_C = ||C||
5:      Using n_C and Map 1, determine fraction of α_max, x_α
6:      Using n_C and Map 2, determine the CR slope magnitude,
        m_CR
7:      Determine α_max as outline with (2)
8:      Determine step length α = x_α α_max
9:      Determine ĝ = S^T C              ▷ Linear back projection
10:     Evaluate CR using (3) and its slope m
11:     while |m| > m_CR do
12:         ĝ ← ĝ − αS^T (Sĝ − C)       ▷ Landweber iteration
13:         Evaluate CR using (3) and its slope m
14:     end while
15:     return ĝ                         ▷ Reconstructed image
16: end procedure
```

FIGURE 2. Landweber iteration method with proposed automated stopping procedure based on the slope of the capacitance residual curve. The maps indicated in lines 2 and 3 are shown in Fig. 5 for the current experimental setup. Linear and spline interpolation are used in lines 5 and 6 while using the maps, respectively. Here, C, S, and $\hat{g}$ denote the capacitance vector, the sensitivity matrix, and the reconstructed image vector respectively.

To alleviate this problem, a stopping criterion can be developed for Landweber iteration method based on the capacitance residual expressed as

$$\mathrm{CR} = \frac{\|\boldsymbol{C} - \boldsymbol{S}\hat{\boldsymbol{g}}\|}{\|\boldsymbol{C}\|} \tag{3}$$

where $\|\cdot\|$ is the 2-norm of a vector. The capacitance residual undergoes a monotonic decrease with iteration count. It is possible to define a value of the slope of the residual curve at which the iteration stops, thus defining the stopping criterion. This slope has to be chosen judiciously such that the reconstruction of both high and low fraction cases perform well. An important parameter in this analysis is the capacitance norm $\|\boldsymbol{C}\|$, which resembles the magnitude of the capacitance vector and is a good measure of volume fraction. A frame with higher volume fraction yields a higher value of capacitance norm and vice versa. This stopping procedure is illustrated with an algorithm for the Landweber method in Fig. 2. It begins with importing maps of capacitance norm $\|\boldsymbol{C}\|$ to fraction of the maximum step length $\alpha_{\max}$ and magnitude of the slope of the capacitance residual (CR). The maps are constructed based on observations for a given sensor setup. Two such maps are shown in the first column of Fig. 5. The abscissa of these maps is also a representative of the volume fraction due to its close relationship to capacitance norm. The first map assigns higher values of the step length α for low and high volume fraction frames, which helps them get reconstructed adequately in a reasonable number of iterations. The second map assigns lower values of the CR slope magnitude for low and high volume fraction frames, which implies a higher iteration number for adequate reconstruction. These observations are derived based on the current sensor configuration and flow setup. A change in either of these, such as in electrode shape or number, or the

presence of a different material such as water, would require the maps to be reconstructed. Once the maps are obtained, appropriate values of the step length α and magnitude of the CR slope m_{CR} are determined based on the capacitance norm value $\|C\|$ for a given frame. Then Landweber iteration is launched and CR calculated in each iteration using (3) along with its slope m. The iteration is stopped when $|m| < m_{CR}$ and the iteration number k is recorded for post-processing purposes. It should be noted that a change in flow regime would not affect this automated stopping procedure because it is only sensitive to changes in volume fractions which is taken care of by the maps. The change in flow regime will be taken care of by the image reconstruction algorithm itself which is independent of the stopping procedure. This is illustrated with two experimental setups featuring two different flow regimes in the experimental results section.

C. VELOCITY RECONSTRUCTION

The procedure for velocity reconstruction based on sensitivity gradient is detailed in [2]. The forward problem in this case is given by

$$\frac{\Delta C}{\Delta t} = \left(G^1 \odot F_x\right)v_x + \left(G^1 \odot F_y\right)v_y + \left(G^1 \odot F_z\right)v_z \quad (4)$$

where $\Delta C = C^2 - C^1$ is the change in capacitance between two consecutive frames, Δt is the time difference between the frame captures, (v_x, v_y, v_z) are $N \times 1$ unknown velocity profile vectors, and (F_x, F_y, F_z) are $M \times N$ sensitivity gradient matrices evaluated by taking the gradient of the sensitivity distribution S. The time interval Δt is related to the frame rate as $f_r = 1/\Delta t$. The $M \times N$ image matrix G^1 is defined as $G^1 = [\hat{g}^1 \ \hat{g}^1 \ \ldots \ \hat{g}^1]^T$, where $\hat{g}^1$ is the reconstructed image corresponding to frame C^1. Here, $\odot$ denotes element-wise product. It is noted that the presence of the G^1 term in the forward equation acts as a spatial masking on the sensitivity gradient fields. As a result, a simple method, such as linear back projection (LBP) provides a reasonably good solution. Now, defining the product terms as $G^1 \odot F_x = f_x$, $G^1 \odot F_y = f_y$, $G^1 \odot F_z = f_z$, LBP can be applied as follows

$$\left(\hat{v}_{0x}, \hat{v}_{0y}, \hat{v}_{0z}\right) = \left(f_x, f_y, f_z\right)^T \frac{\Delta C}{\Delta t} \quad (5)$$

which provides a good estimate of the unknown vectors except the magnitude being smaller than expected. A secondary reconstruction step is required to obtain a more accurate solution. However, instead of using an iterative method such as Landweber, the LBP solution is simply scaled by a parameter c, i.e.,

$$\left(\hat{v}_x, \hat{v}_y, \hat{v}_z\right) = c \times \left(\hat{v}_{0x}, \hat{v}_{0y}, \hat{v}_{0z}\right). \quad (6)$$

As explained in [20], the Landweber method for velocity reconstruction requires tuning the step lengths which becomes problematic when the flow structure exhibits a lot of variability, which is the case in practice for many flows such as a fluidized bed. The scaling of the LBP solution provides a simple and effective solution to this problem. The scaling parameter c can be determined by minimizing the norm of the mismatch of the two sides of (4), expressed as $\|(\Delta C/\Delta t) - c(f_x\hat{v}_x + f_y\hat{v}_y + f_z\hat{v}_z)\|$. A closed-form solution for this minimization problem is given by

$$c = \frac{(\Delta C/\Delta t)^T \left(f_x\hat{v}_x + f_y\hat{v}_y + f_z\hat{v}_z\right)}{\left\|f_x\hat{v}_x + f_y\hat{v}_y + f_z\hat{v}_z\right\|^2}. \quad (7)$$

Here, distinction is noted between the scaling parameter c and the capacitance vector C, which are in normal lowercase and boldface uppercase letters respectively. It is also noted that the scaling parameter c may assume very high values if the denominator becomes small relative to the numerator. This may result from an under-reconstructed image $\hat{g}$ that goes into the f terms, originating from using fixed step length α and iteration count k for Landweber iteration. This issue will be considered in the experimental results section. An alternative to the scaling parameter approach could be complementing the LBP solution in (5) with velocity magnitudes calculated based on cross-correlation among signals obtained from different electrode layers along the sensor axis, as outlined in [30].

D. SECONDARY QUANTITIES OF INTEREST

The reconstructed image and the velocity profile can be further processed to derive a number of secondary parameters such as the average volume fraction and the axial average velocity. The average volume fraction can be calculated from the reconstructed image $\hat{g}$ as

$$\varphi = \sum_{i=1}^{N} g_i / N \quad (8)$$

where N denotes the number of voxels inside the RoI. The numerator in (8) can be considered as the image mass for the respective frame. The average velocity can be calculated from the reconstructed image $\hat{g}$ and velocity profile $\hat{v}$ by taking the ratio of the image momentum to image mass as

$$v_{\text{avg}} = \frac{\hat{g}^T \hat{v}}{\sum_{i=1}^{N} g_i}. \quad (9)$$

The average velocity corresponds to the net velocity in a frame, as opposed to the velocity profile which contains the spatial distribution of the velocity components. The average velocity could be calculated by simply averaging the velocity profile $\hat{v}$ over all the voxels, however, a ratio of image momentum to image mass is used here instead. The image-velocity product in the numerator helps in balancing out the high magnitudes in the scaling parameter issue described above with the underlying low magnitudes in the image, thus providing a more robust estimate for the average velocity. Equation (9) should be applied individually to each coordinate, i.e., v should be replaced with v_x, v_y or v_z.

III. EXPERIMENTAL RESULTS

A. EXPERIMENTAL SETUP

ECVT has found numerous applications in fluidized bed flow characterization [3], [6], [20], [31]. Fig. 3(a) shows the schematic of the fluidized bed experiment used here, which corresponds to one of the cases in [20]. A 3.5 inch inner diameter insulating pipe contains iron-oxide solid particles of mean diameter 1240 μm, known as Geldart Group D particles. The bed height is 10 inches at rest. Gas is passed through the solid which causes fluidization of the medium. A distributor plate is placed at the bottom of the pipe to ensure a uniform gas-flow throughout the pipe. Below the distributor, there is a conduit which supplies the gas from a flow controller device. Two 6×4 ECVT sensors are mounted on the pipe, one at an elevated position compared to the bed and another at the middle of the bed. The upper sensor captures the solid slugs as they travel up during the fluidization process and remains empty otherwise. The bottom of this sensor is set at 34 inches from the bottom of the bed. The lower sensor captures gas slugs during the fluidization process and remains filled with solid otherwise. A photo of the ECVT sensor is shown in Fig. 1(b). As gas is introduced into the pipe, the solid particles undergo fluidization. At lower gas flow rates, the bed undergoes bubbling. As gas flow rate is increased, it goes into the slugging regime where chunks of solid are lifted along the pipe, which reaches up to a certain height and falls as dilute particles. This goes on in a periodic pattern. Slugging starts at a gas flow rate of 554 standard liter per minute (slpm). A slightly higher flow rate of 592 slpm is set for the present experiment. Capacitance data is acquired during the fluidization process at a rate of 125 frames per second (fps), then up-sampled by a factor of 4, resulting in a frame rate of 500 fps. Along with this, the empty and full data are also collected in stationary conditions when the sensor is empty and filled with solid particles, respectively. The two-phase data is treated with moving average and the single phase data is treated with outlier removal and averaging for suppressing measurement noise [20]. Caution needs to be practiced in selecting the moving average window length as over-smoothing may reduce reconstructed velocity magnitudes. The adjacent and the top-to-bottom electrode pairs are discarded due to high nonlinearity and low signal-to-noise ratio (SNR), respectively, resulting in $M = 180$ total number of measurements.

The recorded two-phase data is first analyzed for selecting the frame range for reconstruction. The norm of the normalized capacitance vector, expressed as $\|\mathbf{C}\|$, is a good indicator of the solid fraction in the RoI and can be conveniently used to select the frame range for reconstruction. The norm plot for the recorded data from the upper ECVT sensor is presented in Fig. 3(b), which shows two complete slugging cycles as understood from the fluctuation in the signals. For regular normalized data, a higher norm value corresponds to higher solid fraction and vice versa. For inverse normalized data [25], a higher norm value corresponds to higher gas fraction and vice versa. The inverse normalization curve

(a)

(b)

(c)
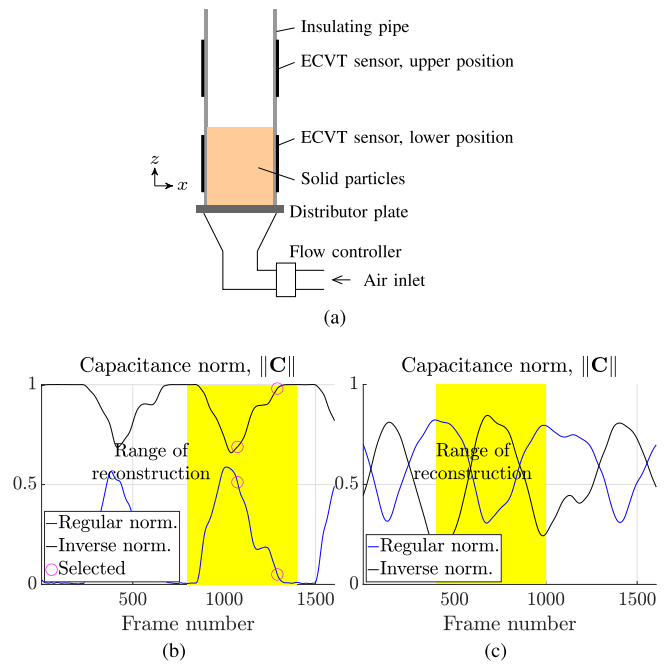
FIGURE 3. (a) Experimental setup of the gas-solid fluidized bed. (b) Signal norm graph for the upper ECVT sensor showing the periodic appearance of solid slugs in the RoI. The yellow rectangle indicates the range of frames selected for image reconstruction. Frames 1073 and 1291 are marked which are used to illustrate the development of the stopping criterion. (c) Signal norm graph for the lower ECVT sensor. This dataset is used for verification of the developed stopping criterion.

is located higher as compared to the regular normalization curve, indicating that the upper sensor remains mostly filled with gas with occasional solid slugs of small fractions. The selected frame range is marked with the yellow region which spans from 800 to 1400, thus including a complete slug cycle. Within the selected frame range, frame 1073 and 1291 are marked, which are used for illustration of the stopping criterion procedure. Those two frames correspond to high and low solid fractions, respectively, thus considering all possible scenarios and are sufficient to evaluate the procedure. The norm plot for the recorded data from the lower ECVT sensor is presented in Fig. 3c. Differently from the upper sensor case, the two norm curves reside in similar ranges, indicating similar solid and gas fractions experienced by this sensor. Thus, the flow regimes are different for the two sensors. For the upper sensor, the solid and the gas phases constitute the dispersed and the continuous phases respectively, which turns the solid phase a suitable candidate for velocimetry. However, this distinction is not so clear for the lower sensor position due to similar fractions of the two phases, therefore, both phases are eligible for velocimetry. Image and velocity reconstruction is more challenging for the upper sensor due to the high dynamic range in the capacitance norm values, which translates to high fluctuations in the respective volume fractions. For this reason, the upper sensor data is used to develop the stopping criterion, whereas the lower sensor data is used for verification purposes.
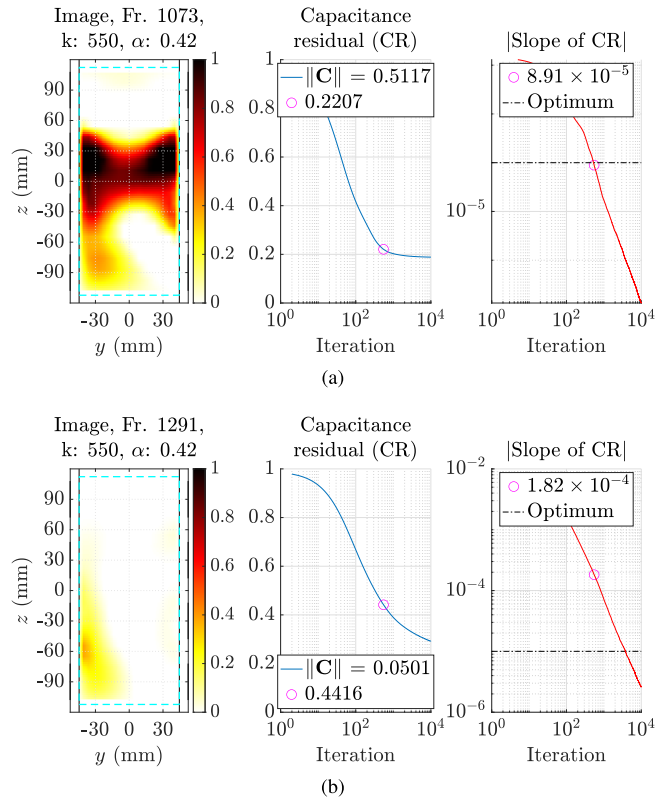
FIGURE 4. Under-reconstruction issue with conventional fixed step length and fixed iteration count method, illustrated with upper ECVT sensor data. Here, k denotes iteration count, α denotes step length, and $\|\mathbf{C}\|$ denotes capacitance norm value. (a) Frame 1073, high volume fraction. The iteration count is chosen such that the capacitance residual value reaches the bend of the curve. (b) Frame 1291, low volume fraction. The iteration count set for the previous frame is not sufficient as the capacitance residual value does not reach the bend of the curve, resulting an under-reconstructed image.
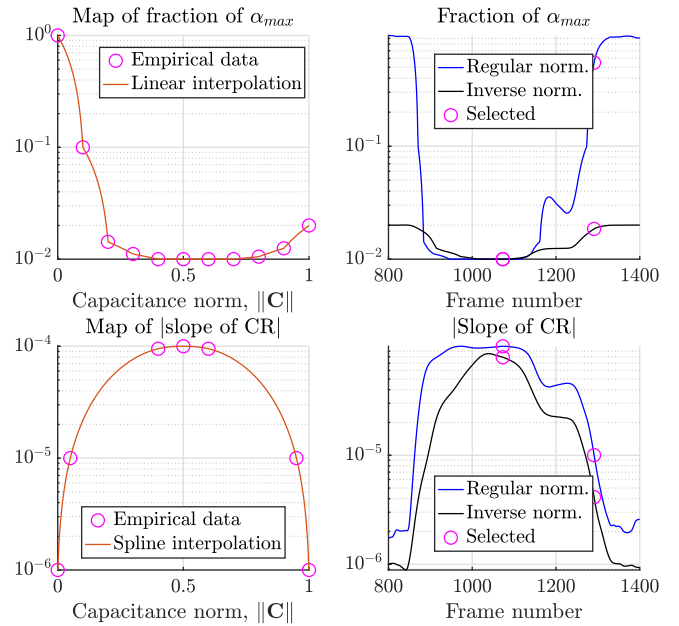

FIGURE 5. Stopping criterion parameters. Upper row: capacitance norm to fraction of α_{max} mapping and the corresponding values over the selected frame range. This mapping assigns higher values of the step length α for low norm frames, which alleviates the under-reconstruction issue with low volume fraction frames. Lower row: capacitance norm to magnitude of slope of capacitance residual (CR) mapping and the corresponding values over the selected frame range. This establishes the stopping criterion, letting the iteration to stop as the slope crosses the threshold.

Here, the expression $\|\mathbf{C}\|$ is normalized with respect to the norm of a all-ones vector of equal length so that it gets bounded in $[0, 1]$. This helps in generalizing the norm based mappings described later. It should be noted that capacitance norm is a good indicator of phase fractions for non-conducting cases such as the present gas-solid case. For conductive media such as water, both capacitance and conductance data are required to be considered [32].

B. DEVELOPMENT OF THE AUTOMATED STOPPING PROCEDURE WITH UPPER ECVT SENSOR DATA

The stopping criterion is developed in this section based on the data from the upper ECVT sensor position as shown in Fig. 3(a). In particular, frames 1073 and 1291 as marked in Fig. 3(b) are used to illustrate the issues with low volume fraction frames originating from using a fixed step length α and iteration count k for Landweber method and how it can be resolved with the present capacitance residual based automated stopping procedure.

1) FIXED STEP LENGTH AND ITERATION COUNT

The use of fixed step length α and iteration count k is illustrated here which has been the conventional method for

stopping Landweber iteration, along with the issues associated with it. These two quantities are set based on observation for a typical frame, which can be a frame with a whole slug in the RoI for the present case. Frame 1073, the high volume fraction frame, is such a frame as understood from the reconstructed image in Fig. 4(a). The step length is set to 0.42, 1/100 of α_{max}, small enough to guarantee convergence. The iteration count is set to 550. Next to the image is the capacitance residual $\|\mathbf{C} - S\hat{g}\|/\|\mathbf{C}\|$ graph which is plotted up to ten thousand iterations. Also printed in the graph is the capacitance norm $\|\mathbf{C}\|$ value which is 0.5117 for this frame. It is observed that around 550 iterations, the monotonic decrease in the residual value changes to a more flat trajectory, indicating the image has been reconstructed to the optimum amount, and thus chosen as the stopping point. The next graph shows the magnitude of the slope of capacitance residual whose value at 550 iterations coincides with the optimum value of slope determined based on a norm-to-slope mapping as shown in Fig. 5, elaborated in the next section. Now, the reconstructed image and other parameters for frame 1291, the low volume fraction frame, is shown in Fig. 4(b) with the same step length and iteration count as frame 1073. The image is under-reconstructed as indicated by the capacitance residual curve whose value has not reached the flat portion of the curve at 550 iterations. More problematic is that the capacitance residual curve has not reached the flat region even with ten thousand iterations. This suggests a bigger step length should have been chosen for this frame, such as α_{max}, however, this might have caused convergence

issues for the other frame. A possible solution is to choose a medium sized step length that is appropriate for frames with all volume fractions, such as 1/10 of α_{max}, however, an elegant solution would be to use a variable step length through a capacitance norm to step length mapping since the former is a good indicator of volume fraction. Such a mapping is shown in Fig. 5. Next to the residual graph is the magnitude of slope graph, showing that the optimum value, determined based on the norm-to-slope mapping shown in Fig. 5, is not reached at 550 iterations. Therefore, using fixed step length and iteration count may cause small volume fraction frames remain under-reconstructed, which in turn may blow up the scaling parameter value due to the denominator getting very small as understood from (7).

2) VARIABLE STEP LENGTH AND ITERATION COUNT

A variable step length and iteration count may solve the issues with the under-reconstructed image described in the previous section. A variable step length can be constructed through a mapping from the capacitance norm to fraction of maximum step length as illustrated with the top-left graph in Fig. 5. For very small, medium, and large norm values, the step length assumes values close to α_{max}, 1/100 of α_{max}, and 1/50 of α_{max}, respectively. These values are marked with circles and set based on observations that frames with lower and higher volume fractions require higher number of iterations for reconstruction as compared to medium ones. The rest of the graph is linearly interpolated. It should be noted that a finer interpolation such as cubic or spline is not necessary as the purpose of this mapping is to just let the iteration reach the flat portion of the capacitance residual curve in a reasonable number of iterations for small volume fraction frames as described above by the issue with Fig. 4(b). The actual stopping criterion will be implemented based on the slope of the capacitance residual graph. As mentioned in Section II-B, the range of values along the ordinate of the map are chosen based on observations with this particular experimental dataset and may require adjustments for a different experimental setup; however, the shape of the map should remain unchanged which is dictated by the relation among the volume fraction of a frame, the step length α, and the iteration count k. Due to the linear relation between the capacitance norm and the volume fraction, this mapping can be considered as a volume fraction to step length mapping as well. The resultant variation in fraction of α_{max} values is plotted in the top-right graph of Fig. 5 as the capacitance norm varies over the selected frame range highlighted in Fig. 3(b). It is observed that for regular normalization, the values are quite different for the two selected frames 1073 and 1291, assuming much higher value for the latter low small volume fraction frame, whereas they are less different for the inverse normalization case. It should be noted that the same mapping can be used for both regular and inverse normalization since the image reconstruction algorithm is not aware of which normalization is chosen. After this adjustment, the step length α remains unchanged
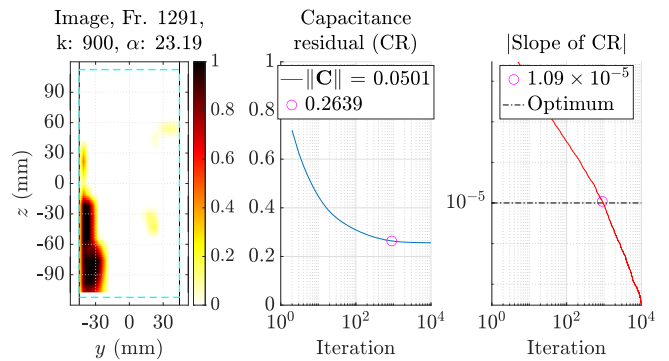

FIGURE 6. Addressing the under-reconstruction issue for the low volume fraction frame by adjusting step length α based on capacitance norm $\|C\|$ with the mapping shown in Fig. 5, which assigns higher values of α for low norm, i.e., low volume fraction frames. These graphs correspond to upper ECVT sensor data.

for frame 1073 and increases to 23.19 for frame 1291. This improves the reconstructed image for the latter, as seen in Fig. 6 when compared to Fig. 4(b). The capacitance residual graph has improved as well, reaching the flat trajectory around 900 iterations. Although the transition is not as sharp as frame 1073 as seen in Fig. 4(a), it is still possible to set a value for the magnitude of the slope which determines the stopping point. This is indicated with the 'optimum' value in the slope graph next.

Therefore, it is possible to set a stopping criterion based on the slope of the capacitance residual curve given that it reaches the flat trajectory in a reasonable number of iterations. Here, the magnitude of the slope is selected for simplicity. It is observed that lower and higher volume fraction frames reaches the optimum at a lower value of slope as compared to medium volume fractions, i.e., the former requires more number of iterations. For this reason, instead of setting a fixed value of slope for all volume fractions, a curved mapping is implemented as shown in the bottom-left graph of Fig. 5. The resultant variation in slope is plotted in the bottom-right graph of Fig. 5 as the capacitance norm varies over the selected frame range as highlighted in Fig. 3(b). It is possible to automate the stopping procedure based on this slope based stopping criterion. A simple conditional check could indicate the stopping point for Landweber method.
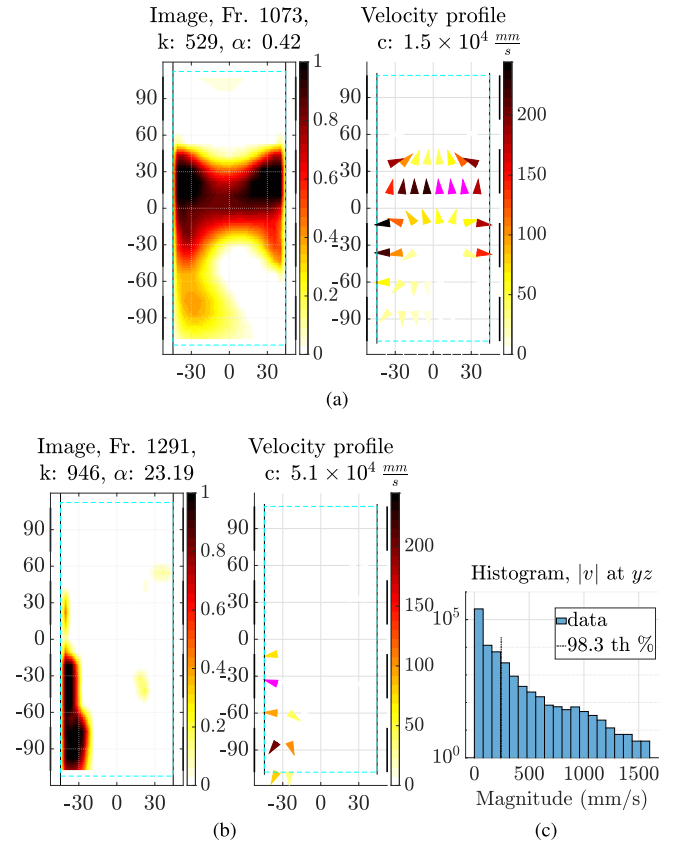
3) IMPROVEMENTS IN IMAGE AND VELOCITY RECONSTRUCTION

Image and velocity reconstruction is conducted for the selected range of frames utilizing the fixed step and the automated stopping procedure described above. The calculated volume fraction using (8) is shown in the upper-left graph of Fig. 7. It is observed that there is a significant increase in solid volume fraction for the automated procedure for low volume fraction frames. The upper-right graph compares the calculated scaling parameter for the two methods, which shows a significant decrease for the solid with low volume fractions for the automated method. This is the most promising improvement as this will eliminate some
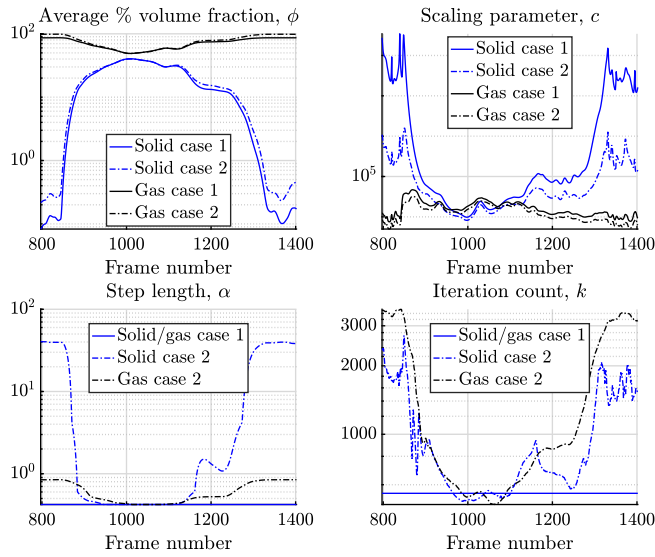
FIGURE 7. Comparing reconstruction parameters for upper ECVT sensor data. Case 1: fixed step length and iteration count. Case 2: variable step length and iteration count with automated stopping. Significant improvement is observed for the latter with the increase in solid volume fraction in the upper-left plot and decrease in solid scaling parameter value in the upper-right plot. The lower plots compare the step length and required iteration counts for the two cases.

FIGURE 8. Image and velocity profile results for the variable step length and iteration count with automated stopping method for the upper ECVT sensor data. Here, k denotes iteration count, α denotes step length, and c denotes scaling parameter. (a) Frame 1073, high volume fraction. Step length is set to low values and lower number of iterations is required. (b) Frame 1291, low volume fraction. Step length is set to high values and higher number of iterations is required. (c) Histogram plot of velocity magnitudes. The 98.3th percentile is marked with a vertical line, which is the colorbar maximum value for the velocity profile plots.

of the high magnitude velocity components from the velocity profile which are primarily artifacts. The resultant step length α and iteration count k are also plotted in the bottom two graphs illustrating the automated functioning of the procedure as opposed to the fixed step procedure. Next, the reconstructed image and velocity profiles for the two selected frames are shown in Fig. 8(a) and 8(b) for the automated procedure. Only the solid phase results are presented as the gas phase information is irrelevant here due to the sensor being filled by gas most of the time. It is observed that frame 1073 is terminated at 529 iterations whereas frame 1291 is terminated at 946 iterations, indicating the automated functioning of the algorithm. The velocity profiles are plotted next to the images for each frame, indicating an upward moving slug for the first frame and a falling dilute solid phase for the second frame. The colorbar next to the graph shows the velocity magnitude scale, with a maximum value of approximately 250 mm/s. It should be noted that the colorbar is mapped to the 0 to 98.3th percentile value of the velocity magnitude distribution corresponding to all the voxels over all the frames. Such a distribution is shown in Fig. 8(c), with the 98.3th percentile value marked with a vertical line, which also corresponds to the colorbar maximum value. Magnitudes above this value are clipped and printed in magenta as observed with some of arrows in the plot. This prevents very high velocity magnitudes from suppressing the rest, thus improving visualization. The high velocity magnitudes in the histogram plot can be traced back to the high scaling parameter values shown in Fig. 7 for the automated procedure. It can be concluded that although significant improvement is achieved in lowering the scaling parameter value for low volume fraction frames, the issue is

not fully mitigated. A more sophisticated procedure might be investigated in future in this respect. From the volume fraction graph in Fig. 7 and the capacitance norm graph in Fig. 3(b), it can be observed that the very low volume fraction frames map to instances as the slug starts appearing into the sensor or disappearing from it. Therefore, it is appropriate to state that the sensor is not reliable in measuring in those instances, or equivalently the sensor is more reliable in measuring if the object is closer to the center. This observation can be utilized in formulating a confidence criterion in interpreting the results.

4) CONFIDENCE CRITERIA FOR INTERPRETING RESULTS

As explained above, the sensor is more reliable in measuring if the object is closer to the center of the sensor. This statement can be quantified with the appropriate superposition of the capacitance norm values corresponding to individual electrode layers, expressed as

$$\psi = w_2\|\boldsymbol{C}_{L2}\| + w_3\|\boldsymbol{C}_{L3}\| - w_1\|\boldsymbol{C}_{L1}\| - w_4\|\boldsymbol{C}_{L4}\| \quad (10)$$
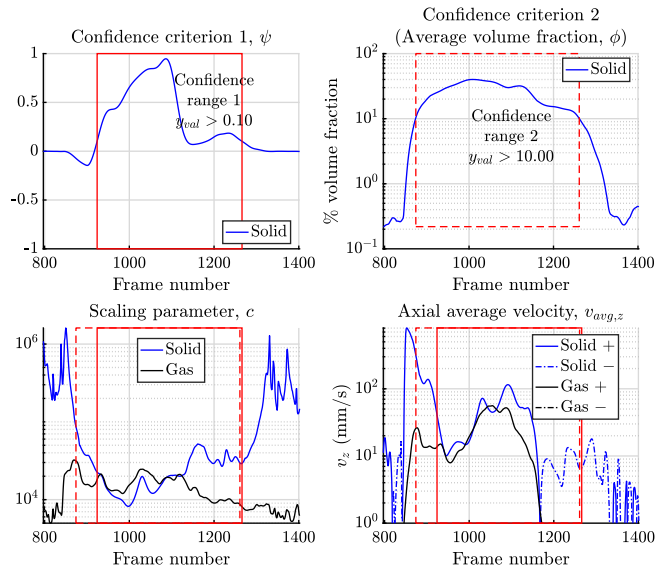
FIGURE 9. Upper ECVT sensor confidence criterion results. Upper row: confidence criterion plots based on superposed per layer capacitance norm values as given in (10) and reconstructed image average volume fraction, respectively. High confidence regions are marked with rectangles based on threshold values. Lower row: indicating high and low confidence regions over the scaling parameter and calculated average velocity graphs. The very high scaling parameter values are successfully assigned low confidence and also the corresponding portion of the average velocity plot. The + and − signs indicate positive and negative values respectively.

where $\|\boldsymbol{C}_{Ln}\|$ denotes the norm of the capacitance vector that contains the electrode pairs in layer n and w_n is the corresponding weight. Layers 2 and 3 are closer to the center whereas layers 1 and 4 are closer to the edge of the sensor. Therefore, this expression is a measure of how close an object is to the center and how far away it is from the edges, thus quantifying the confidence criterion.

Eq. (10) can be considered as a position indicator that automates the tedious task of inspecting thousands of frames manually for evaluating the reliability of the results. The values of the weights can be adjusted to further tune this quantity for specific applications. For the present case, the values are set as $w_2 = w_3 = 1$ and $w_1 = w_4 = 0.2$. The resultant confidence criterion is shown with the upper-left graph in Fig. 9. A higher confidence value is observed with the mid-range frames as opposed to edges, which indicates a higher confidence as the solid slug is closer to the center of the sensor, thus confirming the usefulness of the developed criterion. A threshold of 0.1 is defined to further quantify the level of confidence, which is indicated with a rectangle with red outline that corresponds to a region of higher confidence. This confidence rectangle is printed over the scaling parameter plot in the lower-left corner. It is observed that the very high scale values have fallen outside the rectangle, thus successfully identifying the region with numerical artifacts. Next, this confidence rectangle is printed over the average velocity plot in the lower-right corner, indicating the region of high and low confidence. This plot is generated based on (9). It can be observed that the high velocity magnitudes near the beginning of the plot fall in the low confidence

region, thus successfully discarding the numerical artifacts. It should be noted that there is a strong influence of the weights in determining the confidence rectangle. For example, the rectangle would become narrower if all the weights are set to 1, providing a more strict criterion. Therefore, setting suitable values for the weights needs some amount of tuning and more investigation is required to evaluate the generalization ability of the approach. Lastly, a more simple confidence criterion could be the volume fraction itself as shown with the plot in the upper-right corner. A 10 % threshold is chosen to define the confidence rectangle shown in dashed red outline. This rectangle is printed over the lower two plots and offers a similar characteristic as the previous criterion, however, somewhat relaxed indicated by the extended region at the beginning of the plot.

C. VERIFICATION OF THE AUTOMATED STOPPING PROCEDURE WITH LOWER ECVT SENSOR DATA

The developed stopping criterion in the previous section is verified here based on the data from the lower ECVT sensor position as shown in Fig. 3(a). As explained in Section III-A, the flow regime is different for this sensor position as compared to the upper sensor, thus providing a valid test case to verify the robustness of the method to flow regime changes. The capacitance norm graph is shown in Fig. 3c along with the selected range of frames, for which image and velocity reconstruction is conducted. In particular, the maps shown along the first column of Fig. 5 are used here without any modification. The other reconstruction parameters such as data smoothing, outlier removal etc., described in Section III-A, are adjusted based on the data properties for the present case; however, the channel selection is kept unchanged. The resultant reconstruction parameters are shown in Fig. 10, including volume fraction, scaling parameter, step length, and iteration count. These graphs exhibit similar characteristics as the upper sensor case shown in Fig. 10, except for the changes due to the flow regime transition. The scaling parameter graph shows a decrease in the scaling parameter value for the automated stopping case as compared to the fixed step and iteration case, indicating an improvement. However, this is not as prominent as the upper sensor case due to the simpler flow regime for the present case. Nevertheless, these graphs indicate proper functioning of the automated stopping procedure for the present case, thus verifying the robustness of the method to flow regime changes. Next, the reconstructed image and velocity profiles for a typical frame are shown in Fig. 11(a) for the automated procedure. Different from the upper sensor results shown in Fig. 8, both solid and gas cases are shown here due to their similar volume fractions as observed from the signal norm plot in Fig. 3c. However, the result for the gas case is more reliable for this frame due to the gas being concentrated towards the center, as illustrated with the confidence criterion described above in Section III-B.4. Is is possible to develop a confidence criterion for the present case by properly tuning the scaling parameters of Eq. (10); however,
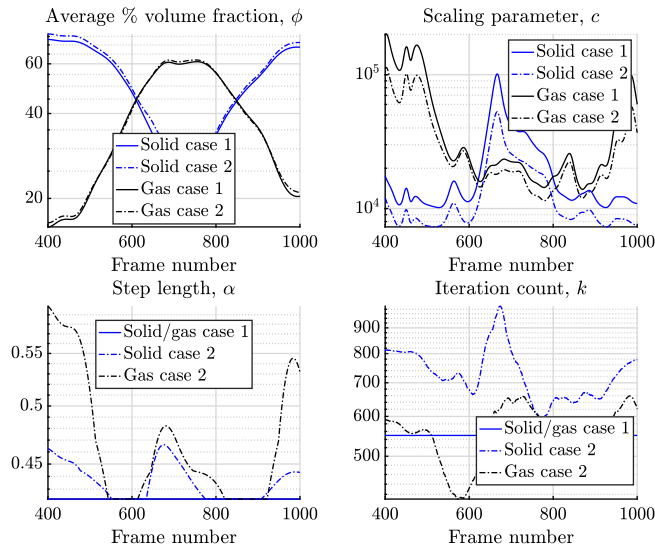
FIGURE 10. Comparing reconstruction parameters for lower ECVT sensor data. Case 1: fixed step length and iteration count. Case 2: variable step length and iteration count with automated stopping method. Improvement is observed for the latter indicated by the decrease in scaling parameter values in the upper-right plot. The lower plots compare the step length and required iteration counts for the two cases. These graphs verify a proper functioning of the automated stopping procedure developed based on the upper ECVT sensor data.
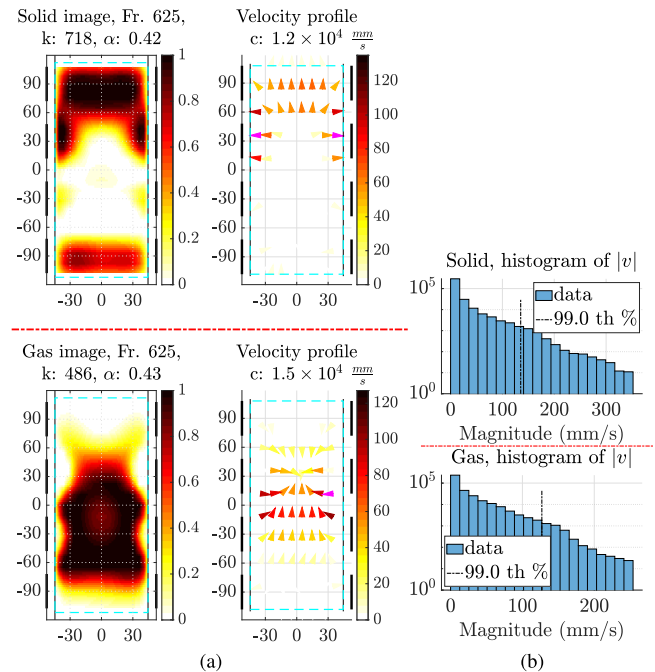
FIGURE 11. Image and velocity profile results for the variable step length and iteration count with automated stopping method for the lower ECVT sensor data. Here, k denotes iteration count, α denotes step length, and c denotes scaling parameter. (a) Top row: results for the solid phase, bottom row: results for the gas phase, indicating a complete gas slug. (b) Histogram plot of velocity magnitudes. The 99.0th percentile is marked with a vertical line, which is the colorbar maximum value for the velocity profile plots.

this is not included here to avoid repetition. The only difference is that the focus would be on both the solid and the gas phases here as opposed to the upper sensor position for which the focus is on the solid phase only. As observed

from the lower velocity profile plot corresponding to the gas phase, it indicates a rising gas slug with maximum velocity of 120 mm/s, which is smaller than the upper sensor case of 250 mm/s, indicating the slugs undergoing acceleration while travelling upward. Next to this graph are plotted the histogram graphs for the velocity magnitude distribution for the solid and gas phases, indicating a 99.0th percentile value selected as the corresponding colorbar maximums.

IV. CONCLUSION

In this paper, a stopping criterion is proposed for Landweber iteration method used for image reconstruction in electrical capacitance volume tomography (ECVT). The stopping criterion is implemented based on the slope of the capacitance residual curve. The methodology is illustrated based on experimental data from a gas-solid fluidized bed which contains both low and high solid fraction cases, thus accounting for a diversity of scenarios. It is found that the developed stopping criterion improves both image reconstruction and velocity profiling performance. The improvement is particularly strong in the velocity profiling, which is otherwise adversely affected by under-reconstructed images for very low volume fraction cases. Further, a confidence criterion is developed based on capacitance norm values per individual electrode layers, which implements an automated procedure to evaluate the reliability of the results based on the position of the reconstructed image in the sensor. Lastly, the developed automated stopping procedure is verified based on a different dataset derived from the same experiment but with a different flow regime. Finally, some possible future efforts are discussed to improve the proposed methodology.

REFERENCES

[1] Q. M. Marashdeh, F. L. Teixeira, and L.-S. Fan, "Electrical capacitance tomography," in *Industrial Tomography: Systems and Applications*, 1st ed., M. Wang, Ed. Cambridge, U.K.: Woodhead, 2015, ch. 1, pp. 3–21.

[2] S. Chowdhury, Q. M. Marashdeh, and F. L. Teixeira, "Velocity profiling of multiphase flows using capacitive sensor sensitivity gradient," *IEEE Sensors J.*, vol. 16, no. 23, pp. 8365–8373, Dec. 2016.

[3] W. Warsito and L.-S. Fan, "Dynamics of spiral bubble plume motion in the entrance region of bubble columns and three-phase fluidized beds using 3D ECT," *Chem. Eng. Sci.*, vol. 60, no. 22, pp. 6073–6084, Nov. 2005.

[4] F. Wang, Q. Marashdeh, A. Wang, and L.-S. Fan, "Electrical capacitance volume tomography imaging of three-dimensional flow structures and solids concentration distributions in a riser and a bend of a gas–solid circulating fluidized bed," *Ind. Eng. Chemistry Res.*, vol. 51, no. 33, pp. 10968–10976, Aug. 2012.

[5] V. Rimpiläinen, L. M. Heikkinen, and M. Vauhkonen, "Moisture distribution and hydrodynamics of wet granules during fluidized-bed drying characterized with volumetric electrical capacitance tomography," *Chem. Eng. Sci.*, vol. 75, pp. 220–234, Jun. 2012.

[6] J. M. Weber and J. S. Mei, "Bubbling fluidized bed characterization using electrical capacitance volume tomography (ECVT)," *Powder Technol.*, vol. 242, pp. 40–50, Jul. 2013.

[7] A. Wang, Q. M. Marashdeh, B. J. Motil, and L.-S. Fan, "Electrical capacitance volume tomography for imaging of pulsating flows in a trickle bed," *Chem. Eng. Sci.*, vol. 119, pp. 77–87, Nov. 2014.

[8] J. N. Sines et al., "Slurry bubble column measurements using advanced electrical capacitance volume tomography sensors," *Powder Technol.*, vol. 355, pp. 474–480, Oct. 2019.

[9] J. N. Sines et al., "Study of gas-water flow inside of a horizontal passive cyclonic gas-liquid phase separator system using displacement-current phase tomography," *Gravitational Space Res.*, vol. 6, no. 2, pp. 28–43, Jul. 2020.

[10] S. M. Huang, A. B. Plaskowski, C. G. Xie, and M. S. Beck, "Tomographic imaging of two-component flow using capacitance sensors," *J. Phys. E, Sci. Instrum.*, vol. 22, no. 3, p. 173, 1989.

[11] W. Q. Yang, A. L. Stott, M. S. Beck, and C. G. Xie, "Development of capacitance tomographic imaging systems for oil pipeline measurements," *Rev. Sci. Instrum.*, vol. 66, no. 8, pp. 4326–4332, Aug. 1995.

[12] H. Wang and W. Yang, "Application of electrical capacitance tomography in circulating fluidised beds—A review," *Appl. Thermal Eng.*, vol. 176, Jul. 2020, Art. no. 115311.

[13] W. Q. Yang, D. M. Spink, T. A. York, and H. McCann, "An image-reconstruction algorithm based on Landweber's iteration method for electrical-capacitance tomography," *Meas. Sci. Technol.*, vol. 10, no. 11, p. 1065, 1999.

[14] J. D. Jang, S. H. Lee, K. Y. Kim, and B. Y. Choi, "Modified iterative Landweber method in electrical capacitance tomography," *Meas. Sci. Technol.*, vol. 17, no. 7, p. 1909, 2006.

[15] M. J. D. Silva, E. Schleicher, and U. Hampel, "Capacitance wire-mesh sensor for fast measurement of phase fraction distributions," *Meas. Sci. Technol.*, vol. 18, no. 7, pp. 2245–2251, Jun. 2007.

[16] S. M. Chowdhury, Q. M. Marashdeh, and F. L. Teixeira, "Electronic scanning strategies in adaptive electrical capacitance volume tomography: Tradeoffs and prospects," *IEEE Sensors J.*, vol. 20, no. 16, pp. 9253–9264, Aug. 2020.

[17] C. Clason, "Regularization of inverse problems," Feb. 2021, *arXiv:2001.00617*.

[18] S. G. Hubmer, "On stopping rules for Landweber iteration for the solution of ill-posed problems," Ph.D. dissertation, Dept. Industriemathematik, Johannes Kepler Univ. Linz, Linz, Austria, Apr. 2015.

[19] T. Elfving and T. Nikazad, "Stopping rules for Landweber-type iteration," *Inverse Problems*, vol. 23, no. 4, pp. 1417–1432, Jun. 2007.

[20] C. Park et al., "Velocity profiling of a gas–solid fluidized bed using electrical capacitance volume tomography," *IEEE Trans. Instrum. Meas.*, vol. 71, 2022, Art. no. 4504516.

[21] M. Soleimani, H. G. Wang, Y. Li, and W. Q. Yang, "A comparative study of 3D electrical capacitance tomography," *Int. J. Inf. Syst. Sci.*, vol. 3, no. 1, pp. 292–306, 2007.

[22] Z. Ye, R. Banasiak, and M. Soleimani, "Planar array 3D electrical capacitance tomography," *Insight Non-Destruct. Test. Condition Monit.*, vol. 55, no. 12, pp. 675–680, Dec. 2013.

[23] G. Villares, L. Begon-Lours, C. Margo, Y. Oussar, J. Lucas, and S. Holé, "A non-linear model of sensitivity matrix for electrical capacitance tomography," in *Proc. Electrostat. Joint Conf.*, Cambridge, ON, Canada, Jun. 2012, P. R4.

[24] Q. M. Marashdeh and F. L. Teixeira, "Sensitivity matrix calculation for fast 3-D electrical capacitance tomography (ECT) of flow systems," *IEEE Trans. Magn.*, vol. 40, no. 2, pp. 1204–1207, Mar. 2004.

[25] S. Chowdhury, Q. M. Marashdeh, and F. L. Teixeira, "Inverse Normalization method for cross-sectional imaging and velocimetry of two-phase flows based on electrical capacitance tomography," *IEEE Sens. Lett.*, vol. 2, no. 1, pp. 1–4, Mar. 2018.

[26] P. C. Hansen, *Discrete Inverse Problems: Insight and Algorithms* (Fundamentals of Algorithms), N. J. Higham, Ed. Philadelphia, PA, USA: SIAM, 2010.

[27] M. Vauhkonen, D. Vadász, P. A. Karjalainen, E. Somersalo, and J. P. Kaipio, "Tikhonov regularization and prior information in electrical impedance tomography," *IEEE Trans. Med. Imag.*, vol. 17, no. 2, pp. 285–293, Apr. 1998.

[28] Q. M. Marashdeh, W. Warsito, L.-S. Fan, and F. L. Teixeira, "A nonlinear image reconstruction technique for ECT using a combined neural network approach," *Meas. Sci. Technol.*, vol. 17, no. 8, pp. 2097–2103, Jul. 2006.

[29] W. Q. Yang and L. H. Peng, "Image reconstruction algorithms for electrical capacitance tomography," *Meas. Sci. Technol.*, vol. 14, no. 1, pp. R1–R13, Jan. 2003.

[30] L. F. Botton, H. L. de Moura, A. N. Wrasse, D. R. Pipa, R. E. M. Morales, and M. J. da Silva, "Twin direct-imaging sensor for flow velocity profiling in two-phase mixtures," in *Proc. IEEE Sensors*, Oct. 2018, pp. 1–4.

[31] Y. Pottimurthy, D. Wang, C. Park, S. Patil, A. Tong, and L.-S. Fan, "Three-dimensional dynamic characterization of square-nosed slugging phenomena in a fluidized bed," *Particuology*, vol. 67, pp. 35–46, Aug. 2022.

[32] R. K. Rasel, B. Straiton, Q. Marashdeh, and F. L. Teixeira, "Toward water volume fraction calculation in multiphase flows using electrical capacitance tomography sensors," *IEEE Sensors J.*, vol. 21, no. 6, pp. 7702–7712, Mar. 2021.

SHAH M. CHOWDHURY (Member, IEEE) received the B.S. degree in electrical engineering from the Bangladesh University of Engineering and Technology, Dhaka, Bangladesh, in 2012, and the Ph.D. degree in electrical engineering from The Ohio State University, Columbus, OH, USA, in 2021. From 2012 to 2015, he was with Samsung R&D Institute Bangladesh as an Embedded Software Developer. He is currently a Postdoctoral Scholar with the Department of Electrical and Computer Engineering and also with the ElectroScience Laboratory, the Ohio State University. His research interests include electrical tomography methods, industrial flow velocity profiling, and inverse problems.

CODY PARK received the B.S., M.S., and Ph.D. degrees in chemical engineering from The Ohio State University, Columbus, OH, USA, in 2016, 2018, and 2022, respectively. His research interests include multi-phase flow and reaction engineering, fluidization, and energy and environmental systems.

YASWANTH POTTIMURTHY received the B.S. degree from the Birla Institute of Technology and Science, Pilani, India, in 2014, and the M.S. and Ph.D. degrees in chemical engineering from The Ohio State University, Columbus, OH, USA, in 2017 and 2021, respectively. His research interests include multi-phase flow system design and scale-up, fluidization, and process tomography.

QUSSAI M. MARASHDEH (Senior Member, IEEE) received the B.S. degree in electrical engineering from the University of Jordan, Amman, Jordan, in 2001, the M.S. and Ph.D. degrees in electrical engineering from The Ohio State University, Columbus, OH, USA, in 2003 and 2006, respectively, and the M.S. degree in chemical engineering and the M.B.A. degree from the Ohio State University, in 2009 and 2012, respectively. He is the Co-Founder, the President, and the CEO of Tech4Imaging LLC, a startup company aimed with advancing capacitance tomography technology and its applications. His research interests include electrical tomography systems, electrostatics, optimization, multi-phase flow, fluid mechanics, information theory, and inverse problems.

FERNANDO L. TEIXEIRA (Fellow, IEEE) received the Ph.D. degree from the University of Illinois at Urbana–Champaign, Champaign, IL, USA, in 1999. He was a Postdoctoral Associate with the Massachusetts Institute of Technology, Cambridge, MA, USA, from 1999 to 2000.

He joined the Ohio State University (OSU), Columbus, OH, USA, in 2000, where he is currently a Professor with the Department of Electrical and Computer Engineering and is also affiliated with the ElectroScience Laboratory. His current research interests include applied electromagnetics and sensor physics. His contributions have been recognized by many awards, including the NSF CAREER Award, the triennial Booker Fellowship from the U.S. Committee of the International Union of Radio Science, the Outstanding Young Engineer Award from the IEEE Microwave Society (MTT-S), NASA Certificates of Appreciation, several teaching and research awards from OSU, and several paper awards. He served as an Associate Editor for IEEE ANTENNAS AND WIRELESS PROPAGATION LETTERS and *IET Microwaves, Antennas, and Propagation*, and as a Guest Editor for *Remote Sensing*, IEEE JOURNAL ON MULTISCALE AND MULTIPHYSICS COMPUTATIONAL TECHNIQUES, and *Progress in Electromagnetics Research*. He served as the Chair of the Joint IEEE AP/MTT-S Columbus Chapter. He is an Elected Member of URSI Commissions B and F.

LIANG-SHIH FAN received the B.S. degree in chemical engineering from National Taiwan University in 1970, the M.S. and Ph.D. degrees in chemical engineering from West Virginia University in 1973 and 1975, respectively, and the M.S. degree in statistics from Kansas State University in 1978.

He joined the Ohio State University in 1978, where he is currently a Distinguished University Professor and a C. John Easton Professor with the Department of Chemical and Biomolecular Engineering. His current research interests include fluidization and applications, multi-phase flow, particulate reaction engineering, electrical tomography, machine learning, and energy and environmental systems. He is a member of the U.S. National Academy of Engineering, an Academician of Academia Sinica, and a Foreign Fellow of the Chinese Academy of Engineering, the Australia Academy of Technology and Engineering, the Indian National Academy of Engineering, and the Mexican Academy of Sciences. He was a recipient of the International Fluidization Achievement Award, E.V. Murphree Award from the American Chemical Society, the R&D 100 award, and was named one of the "One Hundred Engineers of the Modern Era" by the American Institute of Chemical Engineers. He also served as the Department Chair of the Department from 1994 to 2003. He currently serves as the Editor-in-Chief for *Powder Technology*.